AIChE

Highly Resolved Simulations of Solids Suspension in a Small Mixing Tank

J.J. Derksen
Dept. of Chemical and Materials Engineering, University of Alberta, Edmonton, AB T6G 2G6, Canada

DOI 10.1002/aic.13889
Published online August 1, 2012 in Wiley Online Library (wileyonlinelibrary.com).

Simulations of solid–liquid flow in an agitated tank have been performed. The simulations fully resolve the mildly turbulent liquid flow ($Re \approx 2000$) in the tank, and the spherical solid particles suspended in the liquid. Full resolution of the particles sets the grid spacing and thereby limits the tank size and the number of particles (up to 3600 in this article) that are computationally affordable. The solids volume fraction is some 8%. The lattice-Boltzmann method has been used to solve the flow dynamics; the particles move under the influence of resolved hydrodynamic forces, unresolved lubrication forces, net gravity, and collisions (with other particles, the tank wall, and the impeller). We show the start-up of the suspension process, demonstrate its dependency on a Shields number (that we interpret in terms of the Zwietering correlation) and show the impact of polydispersity on the suspension process. © 2012 American Institute of Chemical Engineers *AIChE J,* 58: 3266–3278, 2012

Keywords: solid–liquid suspension, particle-resolved simulation, mixing tank, lattice-Boltzmann method, turbulent flow

Introduction

Solid particles suspended in liquid flows are very common: rivers carrying sediment, slurries being transported through pipelines, powders being dissolved in water, and crystalline material being formed and growing in agitated crystallization reactors are just a few examples. The dynamical behavior of solid–liquid suspensions is the result of an intricate interplay between the dynamics of the liquid phase and the solids phase, and the research on this topic has a long and rich tradition.[1–4] For a large part, this research effort is driven by practical relevance: the design of pipelines for transporting slurries or the assessment of reactor performance that depends on solid–liquid mass transfer (dissolution, crystal growth, and solids carrying catalytic material for liquid-phase reactions) requires knowledge of how the solids distribute themselves in the liquid phase as a result of hydrodynamic forces, net gravity (or buoyancy), and collisions between the solids, or between solids and bounding walls.

The more interesting situations are those with moderate to high solids volume fractions, solid over fluid density ratios of order one, and solid particle sizes that overlap with fluid dynamics length scales, for example, a turbulent flow with particles larger than the Kolmogorov scale. In such situations, the solid particles feel a complex hydrodynamic environment. Where fluid–solid interactions in gas–solid systems (high density ratios) are dominated by the drag force, liquid–solid systems are governed by a broader gamut of forces[5] that make the latter systems more difficult to model. Furthermore, in dense (i.e., high solids-volume-fraction) suspensions, particles interact strongly with one another, through the liquid and as a result of direct interaction (collisions). This complexity makes it challenging to predict the behavior of dense, agitated solid–liquid suspensions.

There is no universal approach for modeling and simulation of suspension flows. The appropriate methods depend on the flow regime (as estimated based on Stokes numbers, Reynolds numbers, solids volume fractions, density ratios, and possibly particle shapes) and on the levels of detail and accuracy required. An overview of methods (Eulerian–Eulerian, Eulerian–Lagrangian, various ways of dealing with turbulence, point particles vs. resolved particles) is beyond the scope of this article. It is important to note, however, that none of the methods is fully predictive. At various levels, assumptions, submodels, or empirical correlations are needed to account for unresolved parts of the suspension physics (one can think of hydrodynamic force correlations, assumptions regarding the dynamic, two-way coupling of fluid and solid, parameterizations related to continuum descriptions of the solids phase as in kinetic theory of granular matter). Usually the finer (length) scales are parameterized, and the larger scales are resolved. There is, however, also a need for simulations that resolve down to finer scales and require little parameterization. I can think of three main reasons: (1) the relevance of what happens at short length scales for process performance (mass transfer, mechanical load on solids, and liquid deformations); (2) the assessment of existing submodels and assumptions for parameterizing small scales; and (3) the development of new parameterizations.[6,7]

There is obviously a computational penalty for resolving down to finer scales: the physical size of the domains that can be simulated gets limited. In very impressive simulations[8] on resolved solid particles in homogeneous, isotropic

Correspondence concerning this article should be addressed to J.J.Derksen at jos@ualberta.ca.

turbulence, the domain size was typically 32 times the particle size. With sand-grain size particles (order 0.3 mm), this implies a domain with linear size of 1 cm, which is much smaller than typical process equipment operated under turbulent conditions. Limitations on domain size are a reason for using fully periodic boundary conditions in such highly resolved simulations. The simulated domain then is a small sample (a mesoscale sample) of what is happening in a large, essentially unbounded domain, away from walls. The latter is an Achilles heel of such fully periodic mesoscopic simulations: they are not able to directly account for geometric effects (walls, impellers, and internal hardware), and (related to this) it is hard to mimic fully periodic conditions and the macroscale homogeneity they imply in an experiment. At the same time, physical experiments are in great need; highly resolved ("direct") simulations of solid–liquid suspension flow still need validation, because complete resolution of all relevant dynamic scales is not possible. Resolving the flow around individual particles is very well possible; however, resolving, for example, their surface roughness (a typically 100 times finer length scale compared to the particle size) is not. Surface roughness is usually parameterized by a friction coefficient that allows for tangential momentum exchange when two particles collide. Similar resolution issues play a role, when particles are in very close proximity. On fixed computational grids, the hydrodynamic interactions then get under-resolved; adaptive grids are not truly an option for simulating the interactions between a significant number (>10) of particles. On fixed grids, models for lubrication forces are then applied to mitigate these resolution issues.

With the above in mind, highly resolved simulations of dense solid–liquid suspensions in mildly turbulent flow were performed. The geometry (a miniature mixing tank with a linear size of a few centimeters and mm size spherical particles) was designed such that it on one side allows for simulations with resolved particles and on the other side for reproducing it in a laboratory. One goal of this work is to invite experimentalists to mimic the flow systems presented here and to (as detailed as possible) visualize the suspension (liquid and solid) dynamics. Such an interaction between experiment and simulation would help in making thoughtful choices regarding parameterizations and numerics (grid resolution, time step, and numerical method), and (hopefully) in building confidence in highly resolved simulations.

Another goal of this work is to generate insights in the ways solid particles get suspended in (mildly) turbulent agitated tanks; how they are lifted off the bottom (by the mean flow, through turbulence, and through collisions), and how they travel through the tank and interact with the liquid, the impeller, and the other particles. The (given the small tank) modest Reynolds number and high particle size over impeller size aspect ratio makes the results not directly applicable to full-fledged industrial operations involving solids suspension. The mechanisms, however, are to some extent universal and therefore also relevant for larger scale processes.

The work presented here is based on our earlier work on resolved simulations of solid–liquid suspensions (mainly in periodic domains)[7,9,10] and on detailed simulations of mixing.[11,12] Many numerical and verification issues have been discussed in these earlier articles. For turbulent mixing flows, these include validation by means laser Doppler anemometry data[11] and assessment of grid effects.[12] Relatively simple solid–liquid systems were used for verification and validation purposes: experimental validation through particle image velocimetry (PIV) experiments of a single settling sphere[13] and verification through comparing simulation results with analytical solutions under creeping flow conditions.[14,15] These verifications include assessment of the effect of grid resolution.[7,14,15] The insights regarding these earlier works have been used in this article. As a result we will only briefly explain the numerical method and will not perform a grid sensitivity study for the specific flow systems at hand. The focus of the article will be on describing the flow field results, and on understanding how they depend on operating conditions in an experimentally verifiable manner.

The organization of this article is as follows: in the next section, the flow system is defined in terms of its geometry and dimensionless numbers. Subsequently, the numerical procedure is outlined. It is based on a lattice-Boltzmann (LB) method for resolving the liquid flow, an immersed boundary method for representing no-slip conditions at solid surfaces (particle surfaces and the impeller), and hard-sphere collisions between particles. In the "Results" section, first qualitative impressions of the suspension flow are given, and its development toward a dynamically steady state is described. In analyzing the results, we focus on the distribution of solids through the tank and on how the liquid and solids velocity fields interact. The final section summarizes the main findings.

Flow System

The layout of the flow geometry along with a definition of the coordinate system is given in Figure 1. Gravity points in the negative z-direction: $\mathbf{g} = -g\mathbf{e_z}$. The tank has a square cross section with side length L. The height of the tank is $H = 5L/6$. An impeller is placed in the center of the tank's cross section and with the middle of the impeller halfway the height of the tank (i.e., at $z = H/2$). It is a pitched-blade turbine: four flat blades are mounted under 45° on a cylindrical hub that is attached to the shaft. The impeller diameter is $D = 2L/5$. The shaft enters the tank from the top. The impeller rotates with an angular velocity of $\Omega = 2\pi N$ (rad/s) with rotational direction such that it pumps downward. The tank is filled up to a level $z = H$ and closed off with a lid, so that no-slip conditions apply all around.

The tank contains a Newtonian liquid with density ρ and kinematic viscosity ν, and we define the impeller Reynolds number as $\mathrm{Re} = \frac{ND^2}{\nu}$. The tank also contains spherical solid particles. In most of the cases, they are uniformly sized with radius a_0. In one case, a bidisperse mixture of particles is simulated with half of the solids mass contained in spheres with radius a_0, and half in spheres with radius $a_1 = 1.17a_0$ (this may seem to be a minor difference; by volume the difference is significant though: $a_1^3 = 1.59a_0^3$). The solid over liquid density ratio has been fixed to $\frac{\rho_s}{\rho} = 2.5$ (typical for, e.g., glass beads in liquid), except for one bidisperse case with half the solids having $\frac{\rho_s}{\rho} = 2.0$, the other half having $\frac{\rho_s}{\rho} = 3.0$. The solids volume fraction has been set for all cases to $\phi = \frac{V_s}{L^2H - V_i} = 0.083$ with V_s to total solids volume (e.g., $V_s = M\,4\pi a_0^3/3$ for M uniformly sized spheres), and $V_i = 0.0018L^3$ the volume of the impeller plus shaft.

Gravitational acceleration has been nondimensionalized through the introduction of $\theta = \frac{\rho N^2 D^2}{g(\rho_s - \rho)2a_0}$. The group θ we view as a variant of the Shields number $\theta = \frac{\sigma}{g(\rho_s - \rho)2a_0}$ that is widely used to characterize erosion of granular beds by fluid flow.[16] Traditionally, the stress σ is a viscous shear stress

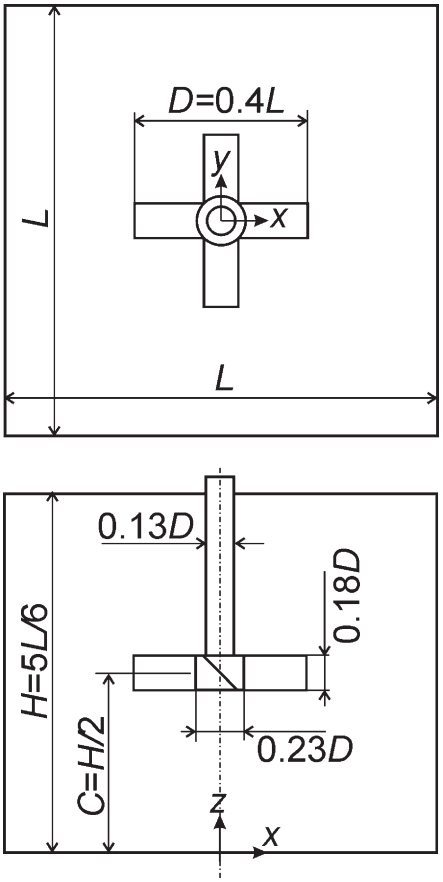

Figure 1. Flow geometry and Cartesian coordinate system.

Top: top view; bottom: side view. The tank is closed off with a lid that acts as a no-slip wall. In addition to the dimensions given in the figure, the thickness of the impeller blades is 0.021*D*. The impeller rotates such that it pumps liquid downward (clockwise in the top view).

(then $\sigma = \rho\nu\dot{\gamma}$ with $\dot{\gamma}$ the shear rate). The Shields number reflects the competition between gravity pulling solids to the bottom of the tank and hydrodynamic stress suspending the particles. As the flow in the tank is dominated by inertia, we have introduced a measure for the inertial stress $\rho N^2 D^2$ rather than a viscous stress in the Shields number.

It is instructive to interpret the above definition of the Shields number in terms of the classical results due to Zwietering[17] on solids suspension in mixing tanks. Zwietering performed an extensive set of solids suspension experiments with particles having a narrow size distribution and summarized the results in a correlation that carries his name. With the symbols as defined earlier the Zwietering correlation reads

$$N_{\mathrm{js}} = s\frac{(2a_0)^{0.2}\nu^{0.1}(100\phi\,\rho_{\mathrm{s}}/\rho)^{0.13}}{D^{0.85}}\left(\frac{g(\rho_{\mathrm{s}}-\rho)}{\rho}\right)^{0.45} \tag{1}$$

with N_{js} the just-suspended impeller speed, that is, the minimum rate of agitation to keep all solids suspended (more precisely defined in Ref. [17]); and s a geometry dependent parameter (in the range 2–20). The term $100\phi\,\rho_{\mathrm{s}}/\rho \equiv \Phi_{\mathrm{m}}$ represents the solids mass fraction as a percentage. If a critical (or just-suspended) Shields number is defined as $\theta_{\mathrm{js}} = \frac{\rho N_{\mathrm{js}}^2 D^2}{g(\rho_{\mathrm{s}}-\rho)2a_0}$, the Zwietering correlation (Eq. 1) can be written as

$$\theta_{\mathrm{js}} = s^2\Phi_{\mathrm{m}}^{0.26}\mathrm{Ar}^{-0.1}\left(\frac{2a_0}{D}\right)^{-0.3} \tag{2}$$

It implies that the critical Shields number depends on the solids mass fraction, a particle size over impeller diameter aspect ratio, and (only weakly; power -0.1) the Archimedes number $\mathrm{Ar} \equiv \frac{g(\rho_{\mathrm{s}}-\rho)}{\rho\nu^2}(2a_0)^3$.

The specific situations that were simulated were chosen based on possibilities for experimental verification (this, e.g., led to the density ratios around 2.5), our desire to have a fairly dense suspension under (mildly) turbulent conditions, and computational feasibility. Computational feasibility limits the number of particles to a few thousand, and it limits the impeller Reynolds number, because all turbulent scales need to be resolved.

We define our base-case in terms of dimensionless numbers in Table 1. As an example of a physical system that has these characteristics, the particles can be assumed to be spherical glass beads with a diameter of 1.0 mm. The impeller then has a diameter of $D = 1.2$ cm, and the sides of the tank are $L = 3.0$ cm. As (on earth) $g \approx 9.8$ m/s^2 and $\theta = 24.0$, the impeller speed is $N = 49.5$ rev/s (roughly 3000 rpm which—in view of experimental feasibility—is a typical drilling speed). To achieve $\mathrm{Re} = 1920$, the kinematic viscosity of the liquid needs to be $\nu = 3.71 \times 10^{-6}$ Pa s (which can be achieved by, e.g., making a glycerol–water mixture).

If we take $s \approx 6$ as an order-of-magnitude estimate for the geometrical parameter in Eq. 1 (see, e.g., the propeller data in Ref. [17]) then $N_{\mathrm{js}} \approx 92$ rev/s (and $\theta_{\mathrm{js}} \approx 83$) for the physical system defined earlier. This is almost twice as high as the base-case impeller speed. As a consequence, we do not expect fully suspended solids for the base-case.

The main variations from the base-case (to be discussed later) are with respect to the Shields number that has been varied in the range $6 \le \theta \le 96$. In the simulations, θ has been varied by varying gravitational acceleration (g); the geometry, impeller speed, and liquid viscosity (and therefore Re) were kept constant. As already mentioned earlier, also bidisperse particle sets were simulated with the spherical particles having different densities or different sizes.

The flow systems are started by creating a random packing of particles on the bottom of the tank. This granular bed has a thickness of approximately $8a_0$, that is, equivalent to four layers of spheres. The impeller is situated well above this bed. Then, the impeller is set to rotate, which agitates the liquid and subsequently causes erosion of the granular bed and solids getting suspended in the liquid. This procedure allows us to study the start-up of the suspension process. It is a scenario that can be mimicked experimentally, albeit with some care related to the speed of image acquisition. As we will see, the start-up phase of the solids

Table 1. Definition of the Base-Case in Dimensionless Numbers

Impeller-based Reynolds number	$\mathrm{Re} = ND^2/\nu$	1920
Number of spheres	M	3600
Solids volume fraction	ϕ	0.083
Density ratio	ρ_s/ρ	2.5
Impeller diameter over sphere radius	D/a_0	24.0
Shields number	$\theta = \frac{\rho N^2 D^2}{g(\rho_{\mathrm{s}}-\rho)2a_0}$	24.0
Tank's height over width	H/L	5/6
Impeller diameter over tank width	D/L	0.4

suspension process takes a few tens of impeller revolutions which (in the physical system) is of the order of a second. On the positive side, the flat side walls of the tank will facilitate visualization of the particles.

Modeling Approach

We used the LB method[18,19] to solve for the liquid flow. The specific scheme used is due to Somers[20]; also see Eggels and Somers.[21] The method has a uniform, cubic grid (grid spacing Δ). The resolution was such that the side length L was represented by 360 grid spacings ($L = 360\Delta$). In fully developed turbulence, the smallest dynamical length scale (the Kolmogorov scale, symbol η) is related to macroscopic length scales (ℓ) via the Reynolds number[22]: $\eta/\ell = \mathrm{Re}^{-3/4}$. If we consider the impeller diameter D as a measure for ℓ, a crude estimate of the smallest turbulent length scale η (crude, because turbulence is not fully developed in our tank operating at $\mathrm{Re} = 1920$) is $\eta = D\ \mathrm{Re}^{-3/4} \approx 0.5\Delta$. Our resolution, therefore, satisfies the typical criterion for sufficiently resolved direct numerical simulations of turbulence: $\Delta < \pi\eta$.[23,24]

The no-slip boundary conditions at the outer walls of the tank were implemented according to the half-way bounce-back rule.[19] The no-slip conditions at the particles' surfaces and at the impeller surface were dealt with by means of an immersed boundary (or forcing) method.[11,13,25] In this method, the surfaces are defined as sets of closely spaced points (the typical spacing between points is 0.7Δ), not coinciding with lattice points. At these points, the (interpolated) fluid velocity is forced to the local velocity of the solid surface according to a control algorithm. The impeller undergoes a predefined rotational motion, so that we know the location and velocity of each of its surface points at any moment in time. The local particle surface velocity has contributions from translational and rotational motion of the sphere under consideration. Adding up (discrete integration) per spherical particle of the forces needed to maintain no-slip provides us with the (opposite; action equals minus reaction) force the fluid exerts on the spherical particle. Similarly, the hydrodynamic torque exerted on the particles can be determined. Forces and torques are subsequently used to update the linear and rotational equations of motion of each spherical particle. This update determines the new locations and velocity of the sphere surface points that are then used to update the liquid flow, and so forth.

It should be noted that having a spherical particle on a cubic grid requires a calibration step, as earlier realized by Ladd.[26] He introduced the concept of a hydrodynamic radius. The calibration involves placing a sphere with a given radius a_g in a fully periodic cubic domain in creeping flow and (computationally) measuring its drag force. The hydrodynamic radius a of that sphere is the radius for which the measured drag force corresponds to the expression for the drag force on a simple cubic array of spheres due to Sangani and Acrivos.[27] Usually a is slightly larger than a_g. The difference $a - a_g$ depends on the kinematic viscosity[26] and is typically equal to half a lattice spacing or less. All simulations presented in this article had the same kinematic viscosity ($\nu = 0.003$ in lattice units; length unit Δ and time unit Δt) and were carried out with a resolution such that $a = a_0 = 6\Delta$ (for $\nu = 0.003$ we then find $a_{g0} = 5.52$). In one of the bidisperse simulations, we have spheres with hydrodynamic radii a_0 and $a_1 = 7\Delta$ (and $a_{g1} = 6.54$).

Experimental validation and grid refinement studies show that a resolution of six lattice spacings over a sphere radius is sufficient for resolving the flow around a solid sphere for particle Reynolds numbers based on slip velocity up to order 50.[13] The particle Reynolds number based on its settling velocity U_∞ for the base-case is $\mathrm{Re}_{p\infty} = \frac{U_\infty 2a_0}{\nu} \approx 25$, that is, less than 50. To obtain this estimate, the Schiller and Naumann[28] drag correlation was used: $C_D = \frac{24}{\mathrm{Re}}\left(1 + 0.15\mathrm{Re}^{0.687}\right)$. An upper bound of the particle Reynolds number in our simulations would be based on a particle slip velocity equal to the impeller tip speed: $\mathrm{Re}_{p,tip} = \frac{\pi ND 2a_0}{\nu} = 400$ which is markedly higher than 50. The impeller tip speed, however, is a measure for the maximum liquid velocity in the tank, and slip velocities (the local difference of liquid and solid velocity) will generally be much smaller than the tip speed. Still, spatial resolution of the flow around the spheres is a concern and will be assessed by determining the way $\mathrm{Re}_p = \frac{u_{slip} 2a_0}{\nu}$ is distributed in the tank for the base-case simulation.

The temporal resolution was such that one revolution of the impeller took 3600 time steps: $N = \frac{1}{3600\Delta t}$. The convective time scales of the particles $\frac{a}{U_\infty}$ and $\frac{a}{\pi ND}$ were $960\Delta t$ and $48\Delta t$, respectively, so that a particle only moves a (very) small fraction of its radius over one time step.

The spheres directly interact through hard-sphere collisions according to the two-parameter model (restitution coefficient e and friction coefficient μ) due to.[29] The same e and μ were also used when a sphere hits one of the bounding walls. Different from gas–solid systems, in liquid–solid systems the choice of the restitution coefficient is not critical for the overall suspension behavior.[7] This is because energy dissipation largely takes place in the liquid phase, not so much during dry collisions between particles. The restitution coefficient was set to $e = 1$ throughout this work. Recent results on erosion of granular beds by laminar flow suggest a more critical role for the friction coefficient.[30] Friction allows particles to exchange angular momentum (or to transfer linear momentum to angular momentum and vice versa) and therefore allows rolling of particles (over one another or over walls). This is relevant for mobilization by fluid flow of solids in granular beds or solids resting on the tank bottom. Our results on erosion[30] show that a zero or a nonzero μ makes a significant difference, with the precise value of a nonzero μ being less relevant (results with $\mu = 0.1$ and $\mu = 0.25$ showed minor differences). As with $\mu = 0.1$ we were able to well reproduce experimental data on critical Shields numbers,[16] that value for μ was used in this work as well.

Collisions between solid spheres and the impeller are modeled according to a scenario akin to soft-sphere collisions: each time step it is checked if sphere volume and impeller volume overlap. If so, we determine the component of the relative velocity of the impeller and the particle in the direction normal to the impeller surface: $u_r = [\mathbf{u_p} - (\Omega \times \mathbf{r})] \cdot \mathbf{n}$ with $\Omega = -\Omega\mathbf{e_z}$ the angular velocity vector of the impeller, $\mathbf{r}$ the location of the particle–impeller contact, and $\mathbf{n}$ the unit outward normal on the impeller surface. At the first detection of overlap the relative velocity is reverted: $\tilde{\mathbf{u}}_\mathbf{p} = \mathbf{u_p} - 2u_r\mathbf{n}$ with $\tilde{\mathbf{u}}_\mathbf{p}$ the postcollision particle velocity. This procedure limits overlap of any sphere with the impeller to 0.5% of the sphere volume at maximum, and the interaction time between sphere and impeller to typically five time steps (0.5° of impeller rotation).

The fixed-grid simulations involving moderately dense suspensions as discussed here require explicit inclusion of subgrid lubrication forces.[31] Assuming creeping flow in between closely spaced spheres, the expression for the radial lubrication force on two solid spheres i and j with center locations $\mathbf{x_{pi}}$ and $\mathbf{x_{pj}}$, radii a_i and a_j, and having relative velocity $\Delta\mathbf{u_{ij}} \equiv \mathbf{u_{pj}} - \mathbf{u_{pi}}$ reads[32]

$$F_{\mathrm{lub}} = 6\pi\rho\nu \frac{a_i^2 a_j^2}{\left(a_i + a_j\right)^2} \frac{1}{s}\left(\mathbf{n}\cdot\Delta\mathbf{u_{ij}}\right), \quad \mathbf{F_{lub,j}} = -F_{\mathrm{lub}}\mathbf{n}, \quad \mathbf{F_{lub,i}} = F_{\mathrm{lub}}\mathbf{n} \tag{3}$$

with s the smallest distance between the sphere surfaces $s \equiv \left|\mathbf{x_{pj}} - \mathbf{x_{pi}}\right| - \left(a_i + a_j\right)$, and $\mathbf{n}$ the unit vector pointing from the center of sphere i to the center of sphere j. The lubrication force on one sphere (say sphere i) in the vicinity of a plane wall follows from Eq. 3 by taking the limit $a_j \to \infty$ and setting $\mathbf{u_{pj}} = \mathbf{0}$. As noted earlier, Eq. 3 is based on a creeping flow assumption in the narrow gap between closely spaced spheres undergoing relative motion and thus is valid if $\mathrm{Re_s} \equiv \frac{s\left|\Delta\mathbf{u_{ij}}\right|}{\nu} \ll 1$. Tangential lubrication forces and torques have not been considered, because they generally are much weaker than the radial lubrication force; the former scale with $\ln\left(\frac{a_i}{s}\right)$, the latter (see Eq. 3) with $\frac{a_i}{s}$. Lubrication forces were not applied for sphere-impeller encounters.

The expression in Eq. 3 has been tailored for use in lattice-Boltzmann simulations according to[31]: (1) The lubrication force needs to be switched off when surfaces are sufficiently far apart in which case the grid associated with the LB method can accurately account for the hydrodynamic interaction between the spheres (typically if $s > \Delta$). (2) The lubrication force needs to saturate when solid surfaces are very close to account for surface roughness and to avoid very high levels of the lubrication force that could lead to unphysical instabilities in the simulations. To achieve Objective (1) instead of Eq. 3 one writes

$$F_{\mathrm{lub}} = 6\pi\rho\nu \frac{a_i^2 a_j^2}{\left(a_i + a_j\right)^2}\left(\frac{1}{s} - \frac{1}{s_0}\right)\left(\mathbf{n}\cdot\Delta\mathbf{u_{ij}}\right) \quad \text{if } s \le s_0, \quad \text{and} \quad F_{\mathrm{lub}} = 0 \quad \text{if } s > s_0 \tag{4}$$

with the modeling parameter s_0 the distance between solid surfaces below which the lubrication force becomes active. For Objective (2), a second modeling parameter s_1 is introduced as the distance below which the lubrication force gets saturated: $F_{\mathrm{lub}} = 6\pi\rho\nu \frac{a_i^2 a_j^2}{\left(a_i + a_j\right)^2}\left(\frac{1}{s_1} - \frac{1}{s_0}\right)\left(\mathbf{n}\cdot\Delta\mathbf{u_{ij}}\right)$ if $s \le s_1$. The settings for s_0 and s_1 were $s_0 = 0.2a_0$ and $s_1 = 2 \times 10^{-4} a_0$. With this procedure and these settings, accurate results for close-range hydrodynamic sphere–sphere interactions have been reported.[7,30,31]

The spheres' equations of linear and rotational motion including resolved and unresolved (i.e., lubrication) forces are integrated according to an explicit split-derivative method.[33,34] These time-step driven updates are linked with an event-driven algorithm that detects and carries out hard-sphere collisions and sphere-outer-wall collisions during the Euler time steps. Once an event is being detected, all particles are frozen, and the event is carried out, which implies an update of the linear and angular velocities of the sphere(s) involved in the event. Subsequently, all spheres continue moving until the end of the time step, or until the next event, whatever comes first. The hard-sphere algorithm has been verified by carrying out granular simulations (no interstitial fluid). Zero-overlap of sphere volumes and exact energy conservation (if $e = 1$ and $\mu = 0$) have been confirmed.[10]

Results

Impressions of the base-case simulation

The way the solids get suspended upon starting the impeller at $t = 0$ is depicted in Figure 2. The figure also shows contours of the liquid velocity magnitude in a vertical mid plane. The downward impeller stream is clearly visible (at least in the $tN = 2$ snapshot). It extends to the granular bed where it is responsible for mobilizing the solid particles in the upper layer of the bed. The erratic structure of the impeller stream shows the transitional/turbulent (or at least the nonlaminar) nature of the liquid flow. After 10 impeller revolutions, many particles have been mobilized. The particles in the four bottom corners, however, have hardly moved at this stage. The base-case simulation was stopped after 50 impeller revolutions when a dynamic steady state was reached as can be witnessed from Figure 3. It shows the average vertical location of the particles and the standard deviation of the vertical particle locations. At the start of the suspension process, the average as well as the standard deviation increase quickly. The average vertical particle location reaches an absolute maximum of approximately $\langle z_{\mathrm{p}} \rangle \approx 0.36H$ after 10 impeller revolutions. It then decreases to a (dynamically) steady-state value of around $0.3H$. The overshoot is a clear manifestation of two-way coupling between liquid flow and solid particle motion: the liquid flow weakens as a result of the presence of suspended particles, because next to liquid, the impeller has to pump around (relatively heavy and inert) particles. The weakening of the liquid flow is not instantaneous due to finite inertia of liquid and solids; it takes time for the suspension flow to adapt itself to changing conditions. Some of the trends in the average vertical particle location can be linked to specific events. For instance, the relatively quick decline around $tN = 20$ is due to the collapse of stacks of particles in the bottom corners of the tank. The time scales of the slow fluctuations in the standard deviation of vertical particle positions (Figure 3) are comparable to those of the average position. The standard deviation does not show an overshoot.

Above we expressed concerns regarding the resolution of the flow around the spheres. To check this further, the distribution of particle Reynolds numbers based on the slip velocity is given in Figure 4. There we show four distributions that are very similar. They relate to two independent instantaneous realizations of the flow and two ways for estimating the liquid velocity in the spheres' vicinity. To determine the slip velocity, the liquid velocity in the vicinity of each sphere was spatially averaged in a cubical volume with its center coinciding with the center of the sphere and with side lengths $3a$ and $4a$ (as indicated in Figure 4). We only averaged the velocity in the part of the cube volumes not occupied by solid. It can be concluded that at any moment some 20% of the spheres has $\mathrm{Re_p} > 50$, which could indicate some lack of spatial resolution.

In Figure 5, the start-up of the solids suspension process is provided in terms of evolutions of vertical, solids-related profiles in the tank. At all times, high solids concentration near the bottom indicates that the solids do not get fully suspended which—in the light of the above discussion related

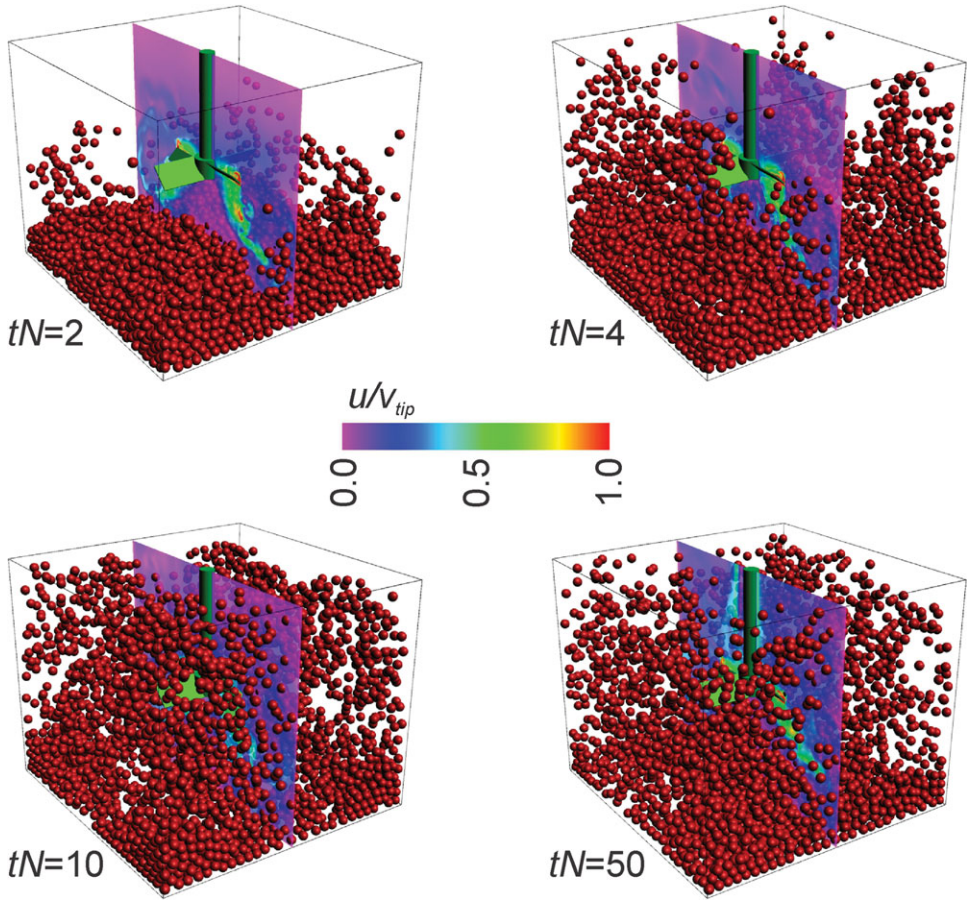

Figure 2. Evolution of the solids suspension process: instantaneous realizations of particle locations and liquid flow (velocity magnitude in the mid-plane) at four moments as indicated.

Base-case conditions. [Color figure can be viewed in the online issue, which is available at wileyonlinelibrary.com.]

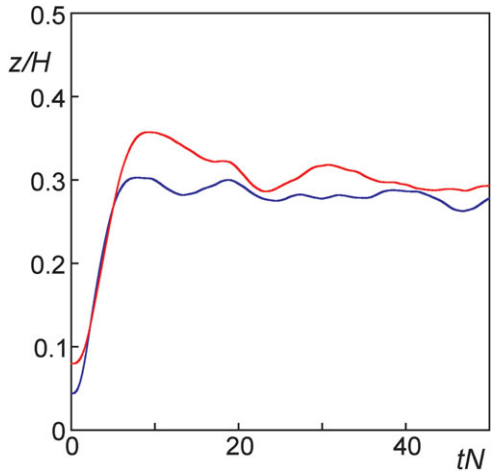

Figure 3. Time series of the average vertical location of the particles $\langle z_p \rangle \equiv \frac{1}{M}\sum_{i=1}^{M} z_{pi}$ (red line) and the rms value of the vertical particle location $\langle z'_p \rangle \equiv \sqrt{\frac{1}{M}\sum_{i=1}^{M}\left[z_{pi} - \langle z_p \rangle\right]^2}$ (blue line).

Base-case conditions. [Color figure can be viewed in the online issue, which is available at wileyonlinelibrary.com.]

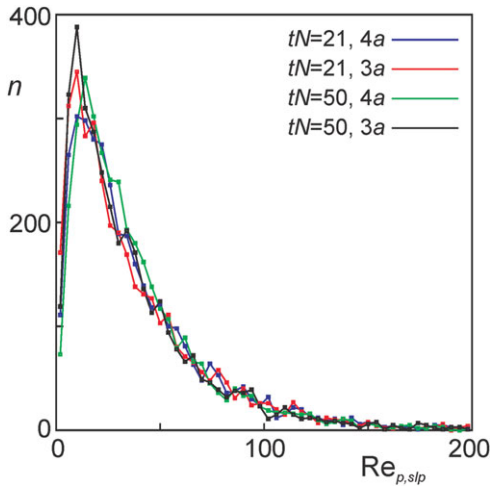

Figure 4. Distribution of particle Reynolds numbers based on the particle–liquid slip velocity $\mathrm{Re}_{p,slp} = \frac{|u_p - u|2a}{\nu}$ at two instantaneous realizations of the flow (21 and 50 impeller revolutions after start-up).

The liquid velocity u was the average velocity in the surroundings of the solid particle. As the surroundings, cubes with sides $3a$ and $4a$ around the particles were considered. Base-case conditions. [Color figure can be viewed in the online issue, which is available at wileyonlinelibrary.com.]

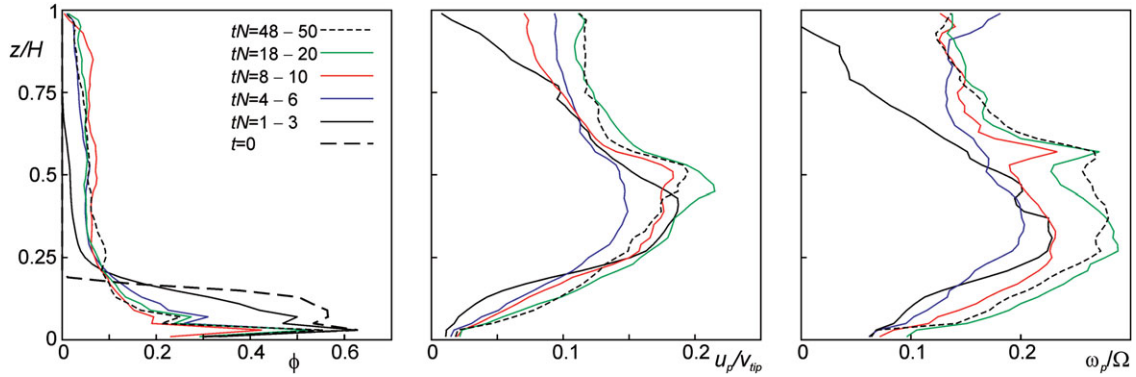

Figure 5. Vertical profiles of (from left to right) average solids volume fraction, average absolute particle linear velocity, and average absolute particle angular velocity at five stages in the suspension process (plus the initial solids distribution).

Averages were taken over time (two revolutions per stage as indicated) and over horizontal slices through the tank. Base-case conditions. [Color figure can be viewed in the online issue, which is available at wileyonlinelibrary.com.]

to the Zwietering[17] correlation—was to be expected for the base-case Shields number of $\theta = 24$. It is interesting to see that the solids volume fraction profile establishes itself much quicker than the particle linear and rotational velocities; specifically in the region above the impeller. Another striking feature is the steep increase in particle rotation rates from above to below the impeller. The down-pumping impeller induces strong shearing motion in the liquid that makes particles rotate. The surface velocity of the particles is, however, dominated by their translational velocity. At the level of the impeller, the average surface velocity due to rotation is some eight times smaller than due to translation: $\omega_p a_0 \approx 0.3\Omega a_0 = 0.025\Omega\frac{D}{2} = 0.025 v_{tip}$ vs. a translational velocity of approximately $0.2 v_{tip}$.

Time-averaged results to be presented here are based on the time window between $tN = 20$ and $tN = 50$, which is deemed sufficiently long for statistically meaningful results. During this time, the suspension is fairly but not completely steady; the average vertical particle location (Figure 3) shows an overall downward trend, albeit a weak one. The time-averaged distribution of solids is given in Figure 6. The vertical cross section shows preferential solids locations underneath the impeller and closely above the bottom of the tank. The latter confirms the not-fully-suspended state of the solids. The horizontal cross section closely above the bottom (at $z = a$) reveals the action of the impeller stream sweeping particles over and away from the bottom. Particles are (on average) removed from the bottom in the middle of the edges where the impeller stream is felt strongest; they collect in the corners and in the center on the tank bottom. Average liquid and solids velocity magnitudes are shown in Figure 7. The overall structure of the two velocity fields is very similar. The high-velocity region of the liquid is slightly bigger than that of the solids that we attribute to solids inertia (the particles need time to speed up when entering the impeller swept volume) and the fact that solids collide very frequently (thereby dispersing momentum) in the impeller stream underneath the impeller.

Shields number effects

The value of the Shields number dominates the suspension process as shown in Figure 8. For $\theta = 6$, solids only get marginally suspended whereas for $\theta = 96$ a seemingly near-uniform solids distribution is achieved (note, however, the collection of particles in the bottom corners for the latter case). The observations in Figure 8 are reflected in the time series of Figure 9 with a clear positive trend of the average vertical particle position with θ. The width of the vertical solids distribution (as expressed by the rms value z_p') is much less sensitive to θ. The time series for $\theta = 6$ is shorter than the others, because this case is computationally much more intensive than the others. The granular bed on the bottom of the tank gets only marginally mobilized and the locally high solids volume fractions induce many collisions that significantly slow down the simulations. In showing time-averaged profiles we will further discard the $\theta = 6$ case.

In the time-average vertical profiles (Figure 10), the different Shields numbers show markedly different solid volume fraction curves (left panel) with the peak level close to the bottom (at $z = a$) reducing by more than a factor of 2 when going from $\theta = 24$ to $\theta = 96$. Remarkably, however, the particle velocities (center panel) and rotation rates (right panel) are not very sensitive to θ.

As Zwietering[17] formulated just-suspended conditions in terms of what happens with the particles at and closely above the bottom, we now focus on the particle behavior there. We define particles at the bottom of the tank as particles having $z_p \leq 1.01 a_0$, that is, the surface of the particle is within 1% of its radius away from the bottom surface. The distribution function of the velocity magnitude of the near-bottom particles at various θ is given in Figure 11 (left panel). Also the distribution of times τ during which particles are lying "still" (i.e., have a very small velocity $|\mathbf{u_p}| \leq 5 \times 10^{-3} v_{tip}$) is presented (right panel). We see significant, however, gradual differences between $\theta = 24$, 48, and 96 (more particles are lying still longer at the bottom for $\theta = 24$ compared to higher θ). We do not observe a clear transition, for example, between nonsuspended and just-suspended.

As an example of the wealth of detailed information regarding solids behavior available through the simulations, we show in Figure 12 average solids data conditioned upon the impeller angle (angle-resolved averages). The figure shows regions in the wake of the impeller blades void of particles, and the strong downward particle velocity induced by the impeller, most notably near the impeller tip. This downward velocity in the center region is compensated for by an overall upward particle velocity near the edges of the tank.

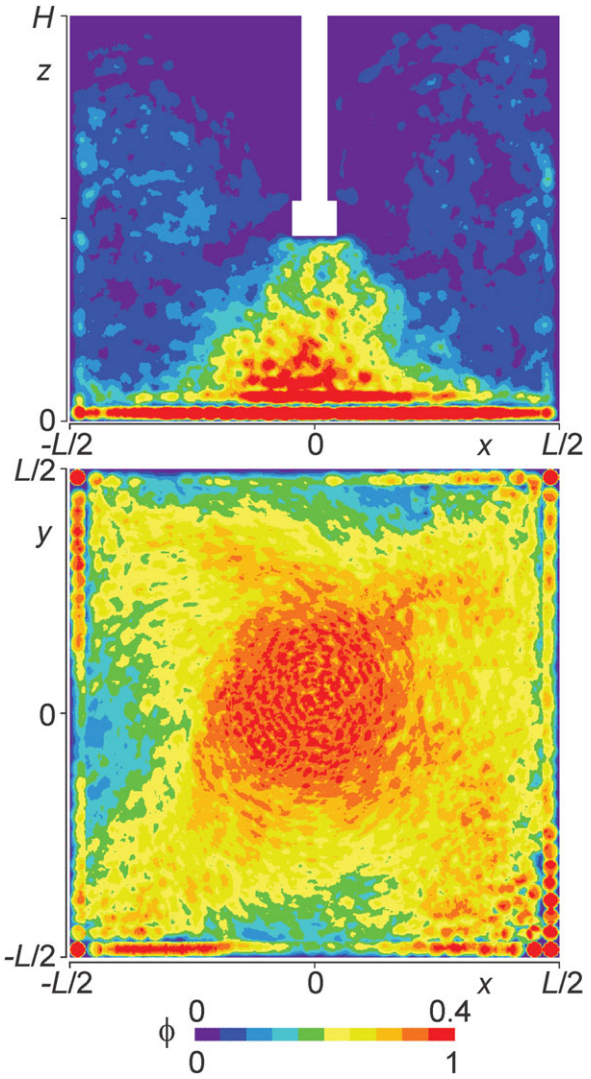

Figure 6. Time-average solids volume fraction in the vertical mid-plane (top) and in the horizontal plane with $z = a$ (bottom).

The time window for averaging is $tN = 20$–50. Base-case conditions. The two panels have different color scales: the upper scale for the upper panel; the bottom scale for the bottom panel. In the view of the bottom panel, the impeller rotates in the clockwise direction. [Color figure can be viewed in the online issue, which is available at wileyonlinelibrary.com.]

Bidisperse systems

So far, simulations were discussed with all particles in the tank being identical. We now move to two bidisperse cases. In the first case, all particles still have the same size (all are spheres with radius a_0), but different density: half the particles has $\rho_s/\rho = 2.0$, the other half has $\rho_s/\rho = 3.0$ (on average the solid over liquid density ratio thus still is the default 2.5, the solids volume fraction still is the default $\phi = 0.083$). In the second bidisperse case, half the solids volume is contained in particles with radius $a_0 = 6\Delta$, the other half of the solids volume consists of spheres with radius $a_1 = 7\Delta$. This case has $\rho_s/\rho = 2.5$, and $\phi = 0.083$ again. In the density-disperse case, a Shields number (based on the average solids density) of $\theta = 24$ has been considered. Also in the size-disperse case $\theta = 24$ if we base θ on a_0 (and $\theta \approx 22$ if it is based on the volume-average particle radius).

As before, we start the discussion with a global impression of the suspension, see Figure 13, and we will focus the discussion on the level of segregation of the different types of particles. The difference in density is clearly shown in Figure 13 (left panel) with red (light) particles preferentially being in the upper parts and blue (heavy) particles in the lower parts. Segregation is far less obvious in the size-disperse case (right panel, Figure 13).

Time series of average vertical particle positions are shown in Figure 14. In the bottom panel, three simulations at $\theta = 24$ have been compared: the base-case with monosized particles and the two bidisperse cases. The solids volume fraction and the mass loading are the same for the three cases, which translates in very similar solids mass-averaged vertical particle locations. If we look at average particle positions in the bidensity case (middle panel of Figure 14), we see that the heavier particles on average end up lower in the tank. The time for this segregation to become steady is at least 65 impeller revolutions (at this stage at the end of the simulation the system is not completely steady), starting from the initial conditions that next to zero-velocity has a random mixture of light and heavy particles in the granular bed. The average vertical position of the heavy particles is about half of that of the light particles. Note that the net gravity force (proportional to $\Delta\rho = \rho_s - \rho$) felt by the heavy particles is twice the net gravity of the light particles.

The picture is less intuitive for the bisize simulation (the simulation involving two particle sizes). Here, the bigger (and thus heavier) particles end up on average slightly "higher" in the tank. This can be understood if we look at the way solids volume is distributed over the tank height (Figure 15). If we first zoom in on the bisize results (right panel), it can be seen that the smaller particles have higher probability of being near the bottom, and near the top, compared to the bigger particles. Near the bottom the smaller particles are less easily entrained (picked up) by the fluid flow. Once entrained, they end up higher in the tank, because they are lighter. The distributions of particles in the bidensity simulation follow expected trends with the heavy particles very much more likely to be closely above the bottom and much less likely to be near the top.

Summary and Conclusions

Particle-resolved simulations of solids suspension in a mixing tank have been performed. In the simulations, the (albeit mild) liquid-phase turbulence as well as the flow around each spherical particle is resolved. Next to relevance for practical applications, the choice of flow system (an agitated tank) is also instigated by the possibility of experiments that can closely match the simulation conditions. Comparison of the simulation results with experimental data is deemed important for assessing the quality of the numerical method, the levels of resolution, and the modeling choices that still need to be made. Modeling in our simulations revolves around particles near contact and in contact with one another. When particles are near contact, the liquid flow between spheres gets under-resolved. This has been compensated for by explicitly adding lubrication forces that are based on creeping flow in the gap between the nearby spheres. Surface roughness of spheres in contact has been parameterized by a friction coefficient.

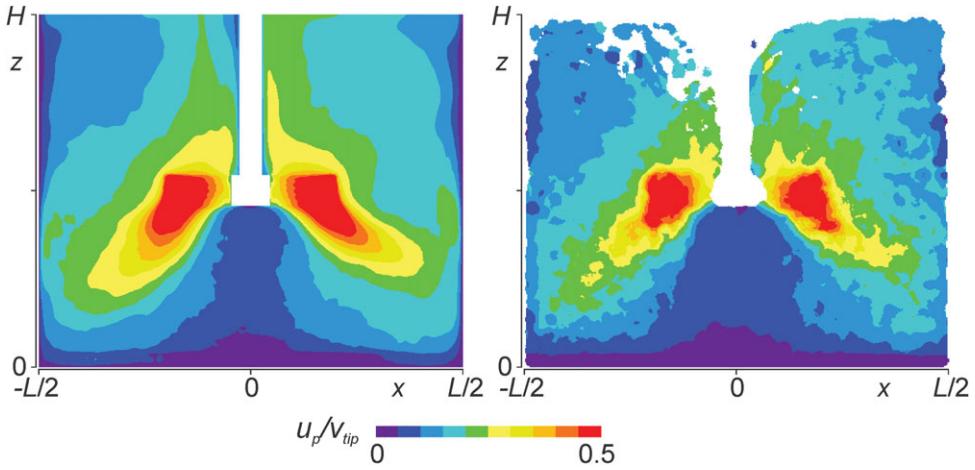

Figure 7. Time-average absolute velocities in the vertical mid-plane.

Left: liquid velocity; right: solids velocity. The time window for averaging is $tN = 20–50$. Base-case conditions. White indicates that no liquid (left, hub and shaft) or no solid (right) was detected there during the time-averaging window. [Color figure can be viewed in the online issue, which is available at wileyonlinelibrary.com.]

Inspired by the Shields number as used in studies of erosion of granular beds,[16] a modified Shields number θ was introduced with a measure for the inertial stress rather than the viscous stress as the driving mechanism for entrainment of solid particles by the flow. The Zwietering correlation[17] was rewritten in terms of a just-suspended Shields number θ_{js}. This form of the Zwietering correlation shows a weak (power -0.1) dependency of θ_{js} on the Archimedes number.

As a monitor of the suspension process, the average vertical solids location $\langle z_p \rangle$ was considered. If the suspension process is started from rest, with the solids forming a granular bed on the tank bottom, $\langle z_p \rangle$ goes through a maximum that is reached

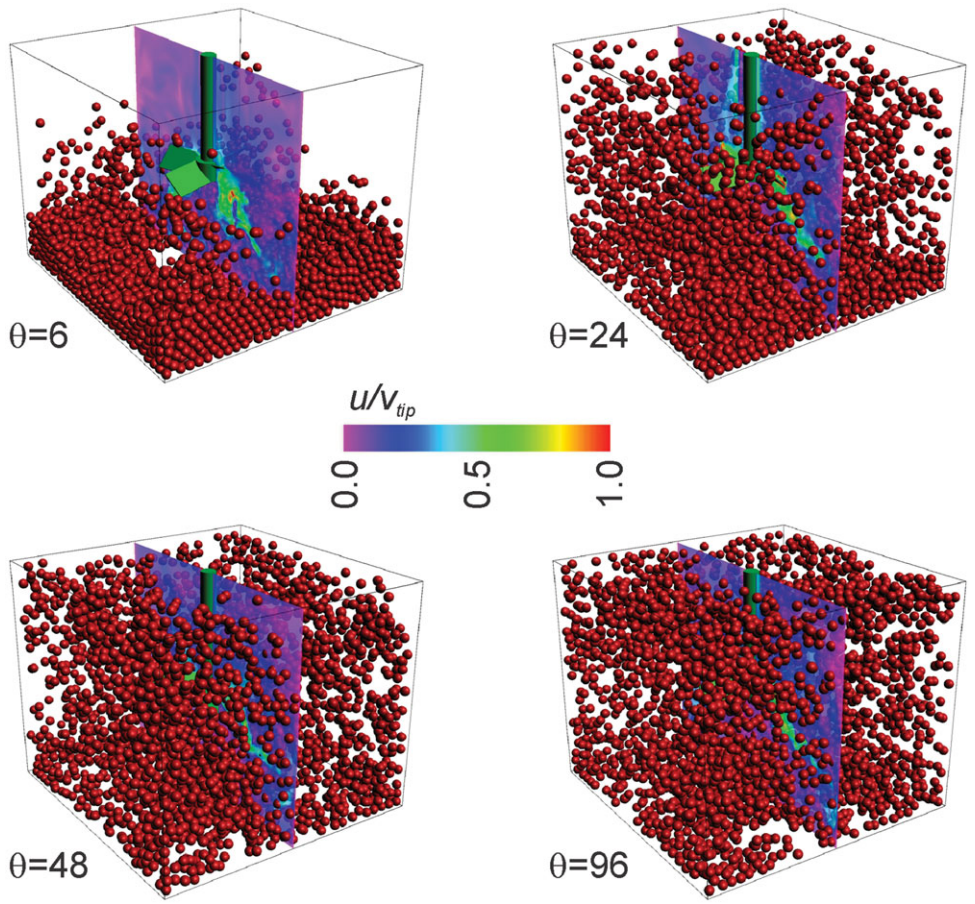

Figure 8. Instantaneous realizations for different Shields numbers θ as indicated after steady state has been reached.

[Color figure can be viewed in the online issue, which is available at wileyonlinelibrary.com.]

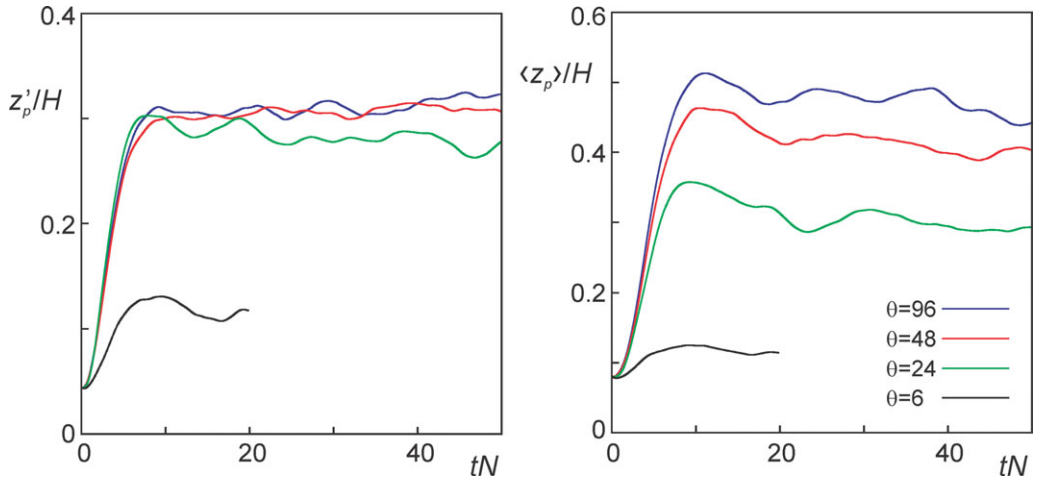

Figure 9. Time series of the average vertical location of the particles $\langle z_p \rangle$ (right panel) and the rms value of the vertical particle location z_p' (left panel) for four values of θ as indicated.

[Color figure can be viewed in the online issue, which is available at wileyonlinelibrary.com.]

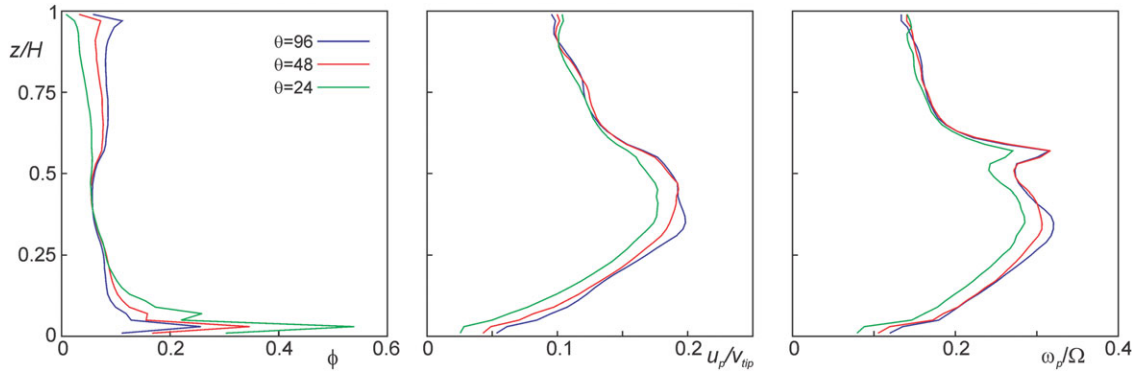

Figure 10. Vertical profiles of (from left to right) average solids volume fraction, average absolute particle linear velocity, and average absolute particle angular velocity for three values of θ as indicated.

Averages were taken over time (from 20 to 50 revolutions after start-up) and over horizontal slices throughout the tank. [Color figure can be viewed in the online issue, which is available at wileyonlinelibrary.com.]

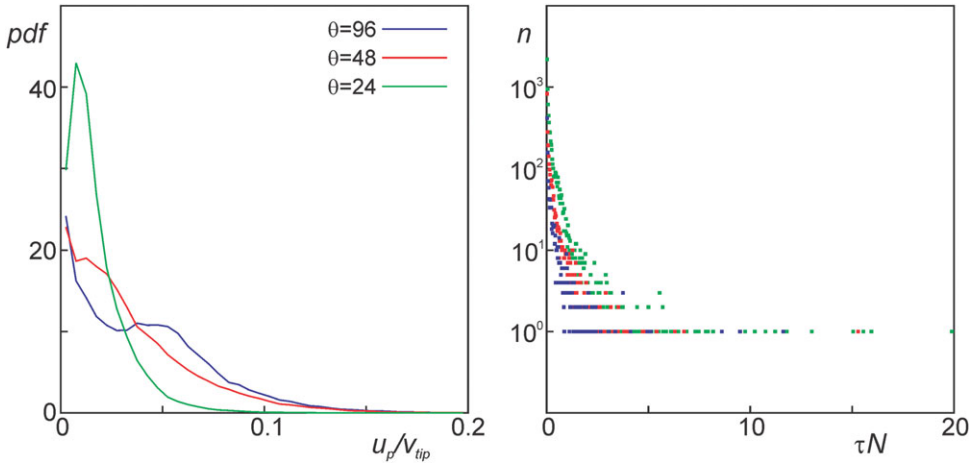

Figure 11. Left: probability density function (pdf) of the velocity magnitude of particles close to the bottom of the tank ($z_p \leq 1.01a_0$).

Right: number of particles lying "still" ($|u_p| \leq 5 \times 10^{-3} v_{tip}$) close to the bottom ($z_p \leq 1.01a_0$) for a time τ. Averages over $20 < tN \leq 50$. In that period on average 16, 6.7, and 3.3% of the particles satisfied the $z_p \leq 1.01a_0$ criterion for $\theta = 24$, 48, and 96, respectively. [Color figure can be viewed in the online issue, which is available at wileyonlinelibrary.com.]

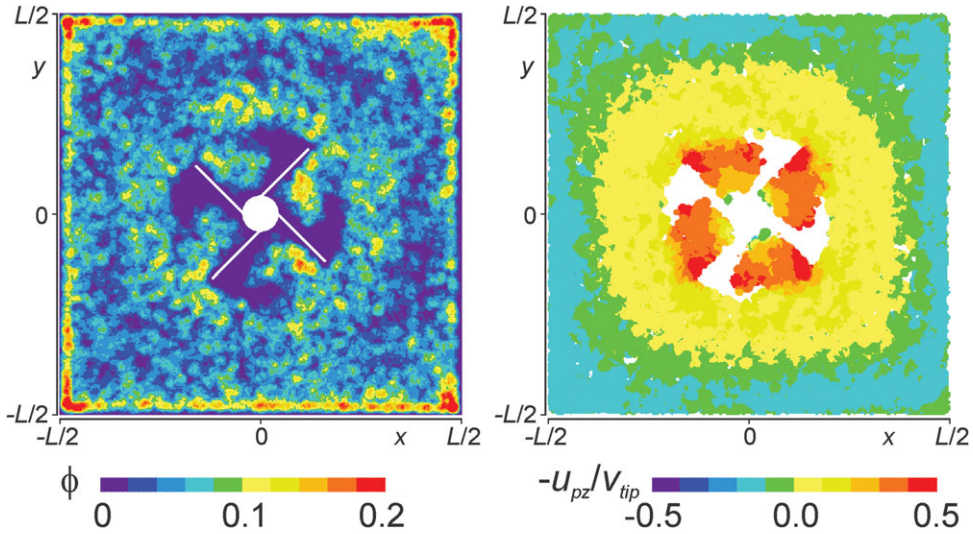

Figure 12. Horizontal cross sections at the lower edge of the impeller; averages conditioned on a 45° impeller position.

Left: solids volume fraction; right: vertical particle velocity. θ = 48. In these views, the impeller rotates clockwise. [Color figure can be viewed in the online issue, which is available at wileyonlinelibrary.com.]

after approximately 10 impeller revolutions. After that, $\langle z_p \rangle$ slowly decays—in about 30 impeller revolutions—to a steady-state value. This overshoot in $\langle z_p \rangle$ we view as a two-way coupling effect: the liquid-only flow initially generated by the impeller is stronger than the suspension flow at later stages.

The suspension process is a pronounced function of θ, with for $\theta = 6$ hardly any particles getting entrained. For θ of order 100 the solids volume distribution over the vertical direction starts to approach uniformity. We do not see, however, a clear transition between not-suspended and just-suspended conditions. Analyses of velocities of particles very close to the bottom only show gradual changes toward increased velocity and less time-at-rest when increasing θ.

The simulation procedure directly accommodates particle size distributions. This was demonstrated by two bidisperse simulations. In the first one, the particles have different density and clearly segregate vertically due to this. In the second bidisperse simulation, the particles have slightly different sizes. The effect of this on their vertical distribution is more subtle compared to the bidensity simulation. Compared to the larger particles, the smaller ones have higher concentration near the bottom and near the top of the tank. The former effect we see as a result of the smaller particles being picked up less effectively by the flow and the latter as a result of their smaller weight.

There are many things that can (and need to) be done to further this research. In the first place we envision experiments that closely match the simulation condition and visualize the suspension process (start-up, steady state). The experimental data would be a great help in making better choices regarding the numerical and modeling aspects of the simulations. In the second place, it would be interesting to add solid–liquid mass transfer to the solution procedure, because this is relevant for the performance of solid–liquid

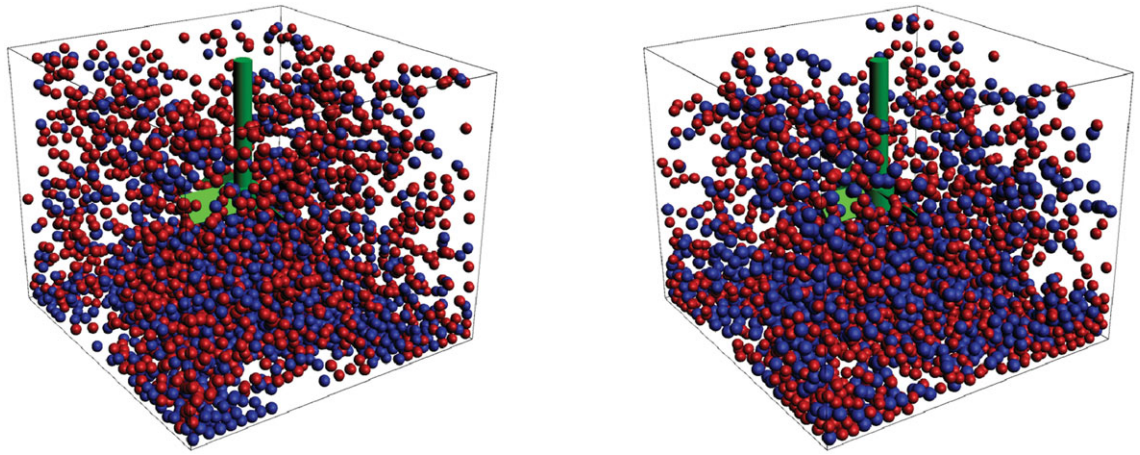

Figure 13. Snapshots of two bidisperse simulations at *tN* = 60.

Left: all spheres have the same radius a_0, the red particles have a density ratio $\rho_s/\rho = 2.0$, the blue particles have $\rho_s/\rho = 3.0$, and $\theta = 24$ (based on the average solids density). Right: red particles have radius a_0, blue particles have radius $a_1 = 1.167a_0$; all particles have the same density ratio ($\rho_s/\rho = 2.5$); the total volume of red and blue particles is the same. [Color figure can be viewed in the online issue, which is available at wileyonlinelibrary.com.]

reactors. This would require solving a passive scalar transport equation (convection-diffusion equation) with the appropriate concentration boundary condition (e.g., equilibrium concentrations) at the particle surfaces. The convection-diffusion equation comes with its own resolution requirements that in the liquid systems are stricter than those for the flow dynamics (the Batchelor scale is a factor $\sqrt{Sc}$ smaller than the Kolmogorov scale with Sc the Schmidt number that is of order 10^3 for liquid systems). In the third place, there are clearly options to port our simulation procedure involving resolved particles to (massively) parallel compute systems. The work presented here was done with a sequential algorithm. Parallelizing this on (say) 1000 cpu's would allow for expanding the linear tank size by a factor of 10 which would bring us in the realm of lab-scale tanks with typically a 30-cm diameter.

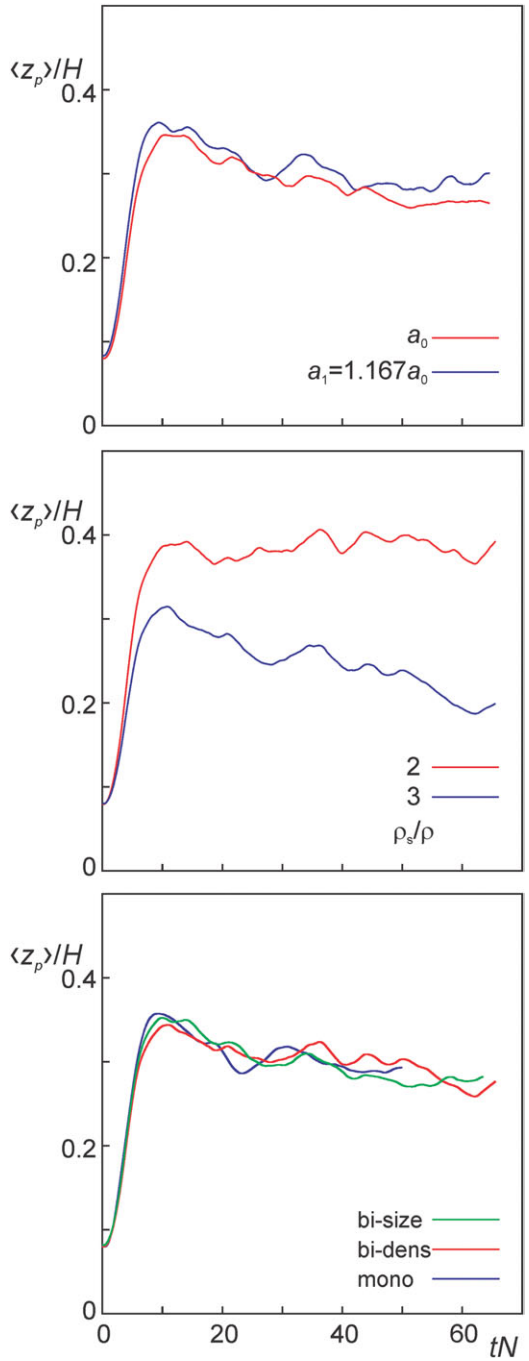

Figure 14. Time series of mass-average vertical particle positions $\langle z_p \rangle$ for $\theta = 24$.

Bottom: comparison between the monodisperse and the two bidisperse simulations with $\langle z_p \rangle$ the mass-weighted average over all particles; middle: average per particle type for the bidensity system; top: average per particle type for the biparticle-size system. [Color figure can be viewed in the online issue, which is available at wileyonlinelibrary.com.]

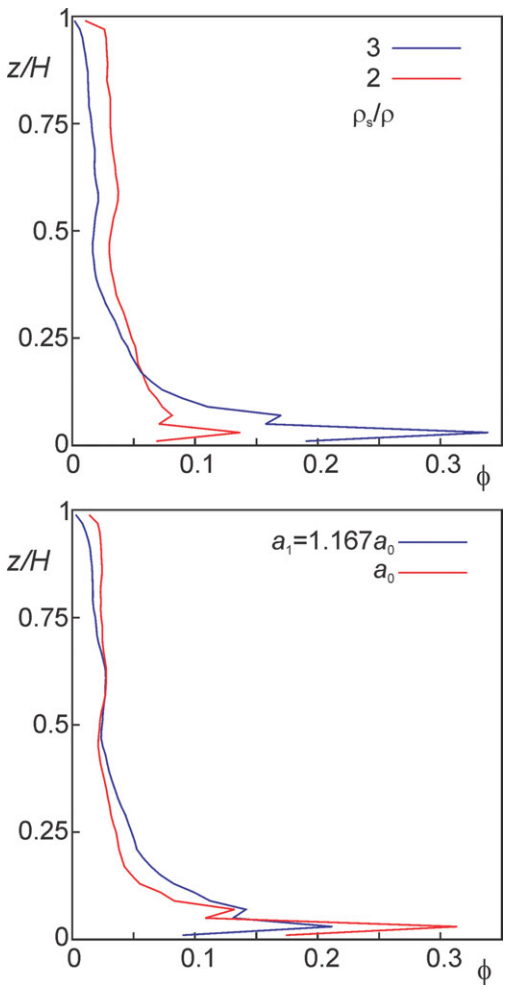

Figure 15. Solids volume fraction per particle type as a function of vertical location *z* for bidisperse simulations.

Left: particles with different densities; right: particles with different sizes. Averages over $40 < tN \leq 63$; $\theta = 24$. [Color figure can be viewed in the online issue, which is available at wileyonlinelibrary.com.]

Literature Cited

1. Stokes GG. *Mathematical and Physical Papers*, *Vols*. I–V. Cambridge: Cambridge University Press, 1901.
2. Richardson JF, Zaki WN. The sedimentation of a suspension of uniform spheres under conditions of viscous flow. *Chem Eng Sci*. 1954;8:65–73.
3. Batchelor GK. Sedimentation in a dilute dispersion of spheres. *J Fluid Mech*. 1972;52:245–268.
4. Guazzelli É, Hinch J. Fluctuations and instability in sedimentation. *Annu Rev Fluid Mech*. 2011;43:97–116.
5. Maxey MR, Riley JJ. Equation of motion for a small rigid sphere in a nonuniform flow. *Phys Fluids*. 1983;26:883–889.
6. Van der Hoef MA, Beetstra R, Kuipers JAM. Lattice-Boltzmann simulations of low-Reynolds-number flow past mono- and bidisperse

arrays of spheres: results for the permeability and drag force. *J Fluid Mech*. 2005;528:233–254.
7. Derksen JJ, Sundaresan S. Direct numerical simulations of dense suspensions: wave instabilities in liquid-fluidized beds. *J Fluid Mech*. 2007;587:303–336.
8. Lucci F, Ferrante A, Elghobashi S. Modulation of isotropic turbulence by particles of Taylor length-scale size. *J Fluid Mech*. 2010;650:5–55.
9. Ten Cate A, Derksen JJ, Portela LM, Van den Akker HEA. Fully resolved simulations of colliding spheres in forced isotropic turbulence. *J Fluid Mech*. 2004;519:233–271.
10. Derksen JJ. Direct numerical simulations of aggregation of monosized spherical particles in homogeneous isotropic turbulence. *AIChE J*. 2012;58:2589–2600.
11. Derksen J, Van den Akker HEA. Large-eddy simulations on the flow driven by a Rushton turbine. *AIChE J*. 1999;45:209–221.
12. Derksen JJ. Blending of miscible liquids with different densities starting from a stratified state. *Comp Fluids*. 2011;50:35–45.
13. Ten Cate A, Nieuwstad CH, Derksen JJ, Van den Akker HEA. PIV experiments and lattice-Boltzmann simulations on a single sphere settling under gravity. *Phys Fluids*. 2002;14:4012–4025.
14. Derksen JJ. Flow induced forces in sphere doublets. *J Fluid Mech*. 2008;608:337–356.
15. Derksen JJ, Larsen RA. Drag and lift forces on random assemblies of wall-attached spheres in low-Reynolds number shear flow. *J Fluid Mech*. 2011;673:548–573.
16. Ouriemi M, Aussillous P, Medale M, Peysson Y, Guazzelli É. Determination of the critical Shields number for particle erosion in laminar flow. *Phys Fluids*. 2007;19:061706.
17. Zwietering ThN. Suspending of solid particles in liquid by agitators. *Chem Eng Sci*. 1958;9:244–253.
18. Chen S, Doolen GD. Lattice Boltzmann method for fluid flows. *Annu Rev Fluid Mech*. 1989;30:329–364.
19. Succi S. *The Lattice Boltzmann Equation for Fluid Dynamics and Beyond*. Oxford: Clarendon Press, 2001.
20. Somers JA. Direct simulation of fluid flow with cellular automata and the lattice-Boltzmann equation. *Appl Sci Res*. 1993;51:127–133.
21. Eggels JGM, Somers JA. Numerical simulation of free convective flow using the lattice-Boltzmann scheme. *Int J Heat Fluid Flow*. 1995;16:357–364.
22. Tennekes H, Lumley J. *A First Course in Turbulence*. Cambridge: MIT Press, 1973.
23. Moin P, Mahesh K. Direct numerical simulation: a tool in turbulence research. *Annu Rev Fluid Mech*. 1998;30:539–578.
24. Eswaran V, Pope SB. An examination of forcing in direct numerical simulations of turbulence. *Comput Fluids*. 1988;16:257–278.
25. Goldstein D, Handler R, Sirovich L. Modeling a no-slip flow boundary with an external force field. *J Comp Phys*. 1993;105:354–366.
26. Ladd AJC. Numerical simulations of particle suspensions via a discretized Boltzmann equation. Part I: Theoretical foundation. *J Fluid Mech*. 1994;271:285–309.
27. Sangani AS, Acrivos A. Slow flow through a periodic array of spheres. *Int J Multiphase Flow*. 1982;8:343–360.
28. Schiller L, Naumann A. Uber die grundlagenden Berechnungen bei der Schwerkraftaufbereitung. *Ver Deut Ing Z*. 1933;77:318–320.
29. Yamamoto Y, Potthoff M, Tanaka T, Kajishima T, Tsuji Y. Large-eddy simulation of turbulent gas-particle flow in a vertical channel: effect of considering inter-particle collisions. *J Fluid Mech*. 2001;442:303–334.
30. Derksen JJ. Simulations of granular bed erosion due to laminar shear flow near the critical Shields number. *Phys Fluids*. 2011;23:113303–1–113303–12.
31. Nguyen N-Q, Ladd AJC. Lubrication corrections for lattice-Boltzmann simulations of particle suspensions. *Phys Rev E*. 2002;66:046708.
32. Kim S, Karrila SJ.*Microhydrodynamics: principles and selected applications*. Boston: Butterworth-Heinemann, 1991.
33. Feng Z-G, Michaelides EE. Robust treatment of no-slip boundary condition and velocity updating for the lattice-Boltzmann simulation of particulate flows. *Comp Fluids*. 2009;38:370–381.
34. Shardt O, Derksen JJ. Direct simulation of dense suspensions of non-spherical particles. In: *Proceedings of ASME-JSME-KSME Joint Fluids Engineering Conference*, 2011; paper AJK2011–19002.

Manuscript received May 4, 2012, and revision received July 9, 2012.